Seasonal Eddy Field Modulation of the North Pacific Subtropical Countercurrent: TOPEX/Poseidon Observations and Theory

BO QIU

Department of Oceanography, University of Hawaii at Manoa, Honolulu, Hawaii

(Manuscript received 15 May 1998, in final form 22 October 1998)

ABSTRACT

Altimetry data from the first 5¼-yr TOPEX/Poseidon mission (October 1992–December 1997) are analyzed focusing on the North Pacific Subtropical Countercurrent (STCC) near the center of the Pacific's western subtropical gyre. The multiyear altimetry data reveal that the eastward-flowing STCC is a highly variable zonal current, whose area-averaged eddy kinetic energy level (338 $cm^2 s^{-2}$) reaches half the eddy kinetic energy level of the Kuroshio Extension. The eddy kinetic energy of the STCC has a well-defined annual cycle with a maximum in April/May and a minimum in December/January. The peak-to-peak amplitude of this seasonal eddy kinetic energy modulation exceeds 200 $cm^2 s^{-2}$. No such distinct annual cycle of the eddy kinetic energy is found in any other zonal current of the North Pacific Ocean. Using a 2½-layer reduced-gravity model representing the vertically sheared STCC–North Equatorial Current (NEC) system, it is shown that the seasonal modulation of the STCC's eddy field is a manifestation in the intensity of baroclinic instability. In spring the STCC–NEC system has a large vertical velocity shear and a weak vertical stratification, subjecting it to strong baroclinic instability. In fall, reduction in the vertical velocity shear between the STCC and its underlying NEC, and intensification of the upper-layer stratification weakens the baroclinic instability. In comparison with the STCC of 19°–25°N, the altimetry data reveal that the westward-flowing NEC existing between 10° and 15°N has a relatively low eddy kinetic energy level, despite being a stronger vertically sheared zonal current than the STCC. That the NEC is less eddy energetic is shown to be due to both its presence in a low-latitude band and its unidirectional flow. Both of these factors make it more difficult to reverse the potential vorticity gradient of the mean state (i.e., satisfying the necessary condition for the baroclinic instability) in the NEC than in the STCC–NEC system.

1. Introduction

The launch of the TOPEX/Poseidon (T/P) satellite in 1992 and its successful multiyear measurements of the sea surface height field provided the oceanography community with an excellent opportunity to study the variability of the world's ocean circulations (Fu et al. 1994; T/P special issues of *Journal of Geophysical Research* of December 1994 and December 1995). In addition to being a useful means to monitor the global sea surface height field on a temporally repetitive basis, the T/P altimetric data are also helpful in revealing new features of the ocean circulation in regions where the variability is heretofore thought to be relatively weak. Figure 1 shows the distribution of the rms sea surface height (SSH) variability in the North Pacific derived from the T/P altimeter data over the past 5¼ years (October 1992–December 1997). High SSH variability regions in Fig. 1 include the Kuroshio/Kuroshio Extension southeast of Japan, the North Equatorial Countercurrent along 5°N, and the region off the Pacific coast of Central America around 11°N. The high SSH variations of this latter region are due to the westward migration of the energetic anticyclonic eddies induced at the Gulf of Tehuantepec and the Gulf of Papagayo (Stumpf and Legeckis 1977; McCreary et al. 1988).

In addition to these well-known current and eddy systems in the North Pacific, Fig. 1 shows a regional maximum of the SSH variability that has an rms value >0.10 m and extends from 135°E to 175°W in a zonal band from 19°N to 25°N. A similar high variability band in the western North Pacific was previously noted by Wyrtki (1975) in his analysis of historical hydrographic data and by Aoki and Imawaki (1996) in their analysis of the Geosat altimetric data. Superposition of this high variability band upon the surface dynamic topography map of the North Pacific (see the dashed box in Fig. 2) indicates that this band is located where the isobaths of the dynamic topography veer eastward near the center of the subtropical gyre. As depicted in Fig. 3, these eastward veering isobaths between 19°N and 27°N cor-

Corresponding author address: Dr. Bo Qiu, Department of Oceanography, University of Hawaii at Manoa, 1000 Pope Road, Honolulu, HI 96822.
E-mail: bo@lunarmax.soest.hawaii.edu

© 1999 American Meteorological Society

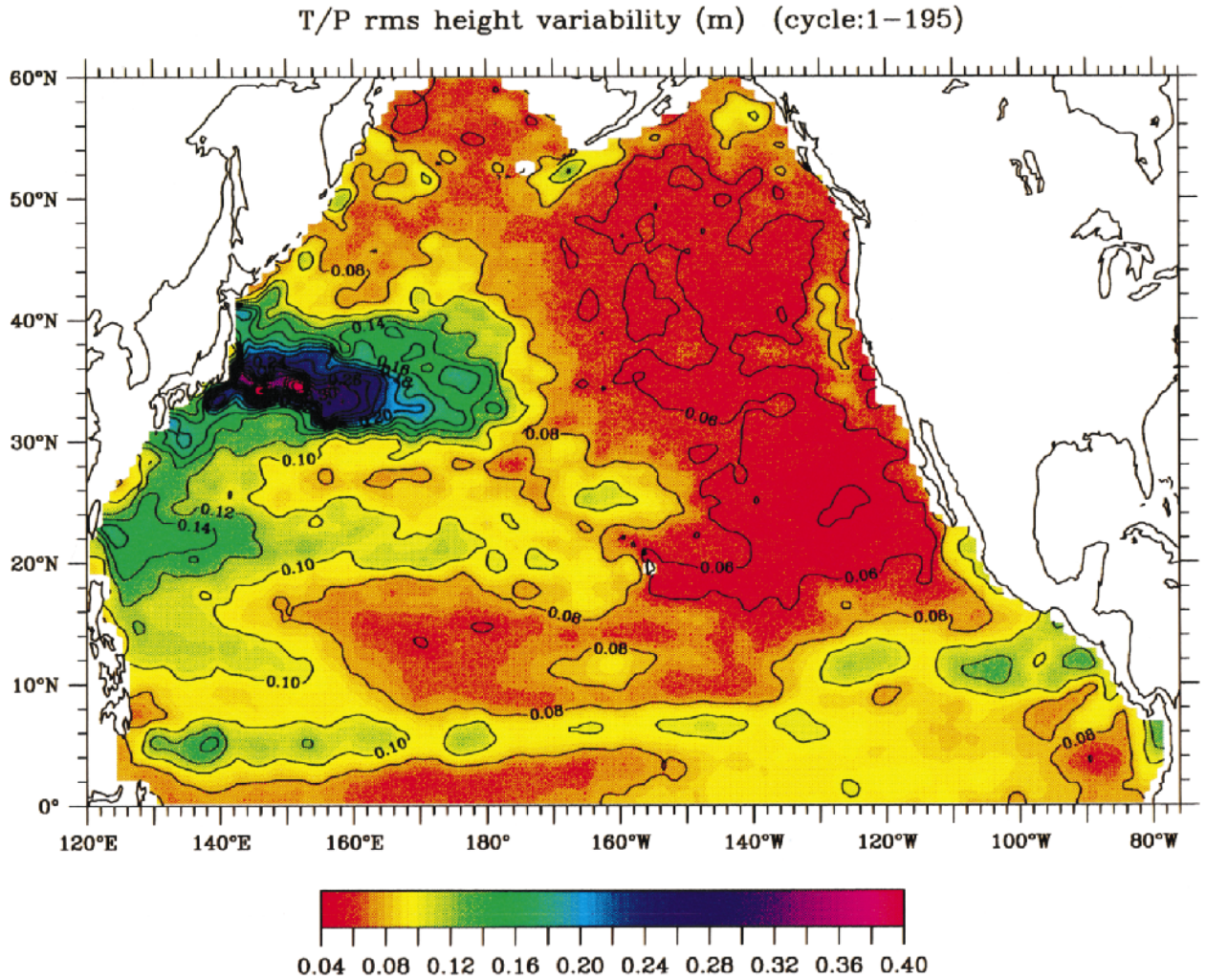

FIG. 1. Map of the rms sea surface height (SSH) variability in the North Pacific Ocean. Based on the T/P altimetric data from October 1992 to December 1997. The rms values are evaluated first along the T/P ground tracks and are mapped subsequently using a Gaussian smoother with the decorrelation scales of 0.5° lat and 1.5° long. No steric height effect is removed.

respond to the surface eastward flow of the North Pacific Subtropical Countercurrent (STCC).

Discovery of the STCC in the western North Pacific subtropical gyre by Japanese scientists dates back to the mid 1960s. By computing the Sverdrup transport from the springtime wind stress data, Yoshida and Kidokoro (1967) predicted the existence of an eastward flow at 20°–25°N in the western North Pacific, a region where one would otherwise expect a westward flow feeding the western boundary current based on the classical wind-driven circulation theory. The presence of this eastward current, which Yoshida and Kidokoro dubbed the STCC, was later confirmed both by Uda and Hasunuma (1969) from direct current meter observations and geostrophic calculations and by White et al. (1978) using historical XBT data.

To place the STCC in the context of the large-scale subtropical circulation, we show in Fig. 4 a typical, meridional temperature cross section observed in the western North Pacific. In this figure, the sharp thermal front at 36°N corresponds to the Kuroshio Extension. The thermocline associated with the Kuroshio Extension is deep, reaching greater than 800 m. The thermocline in between 19° and 27°N has an upper and a lower branch. The upper branch corresponds to the eastward-flowing STCC and the lower branch corresponds to the wind-driven, westward-flowing North Equatorial Current (NEC). Notice that the strong, meridional temperature gradient in the surface layer around 26°N is commonly known as the Subtropical Front (Roden 1975). As shown in Fig. 4 and studies by Roden (1980) and Yuan and Talley (1996), its geographical position is located poleward of 25°N in the western North Pacific. In other words, the high SSH variability band detected by the T/P altimeters (between 19° and 25°N) are associated more with the vertically sheared STCC–NEC system than with the fluctuations of the outcropping Subtropical Front itself.

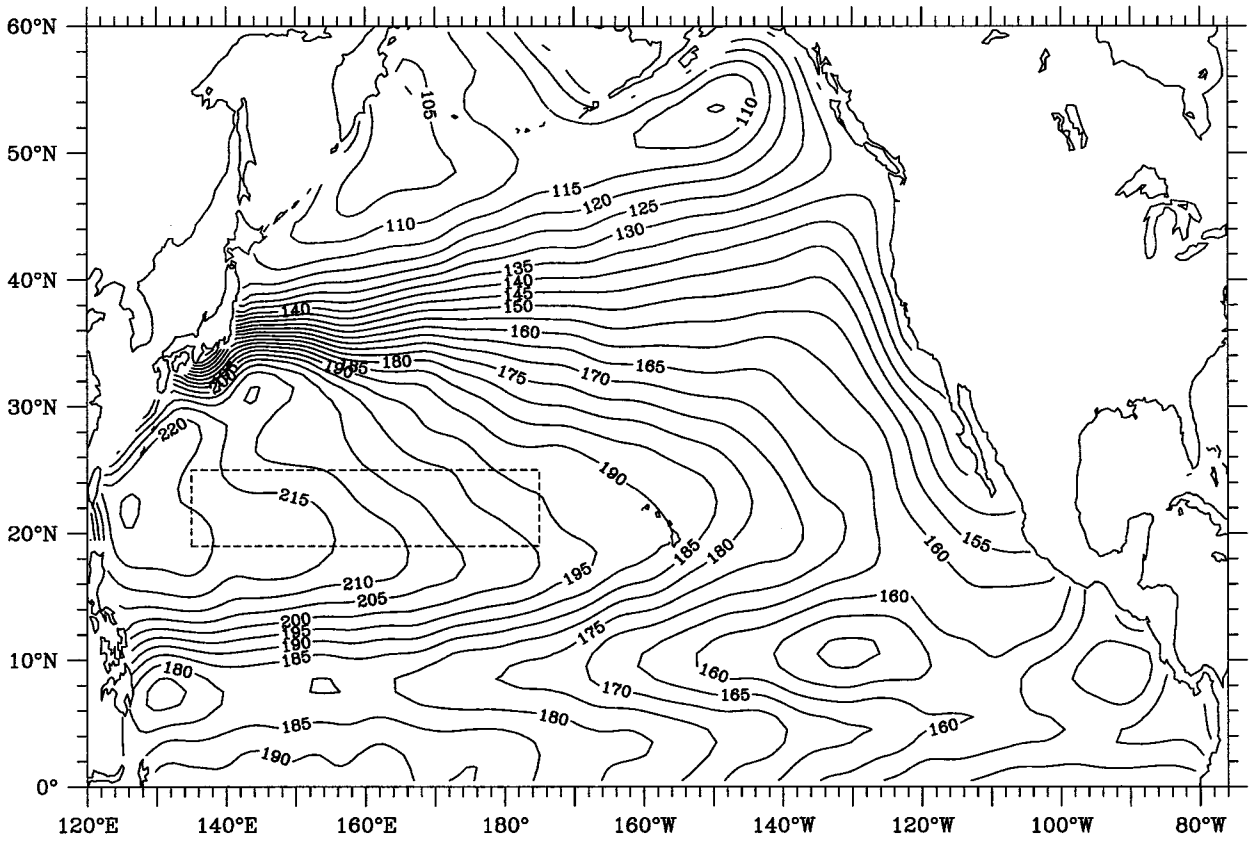

FIG. 2. Mean sea surface dynamic topography relative to 1000 dbar. Units are centimeters. Based on the climatological temperature and salinity (*T*–*S*) datasets of Levitus and Boyer (1994) and Levitus et al. (1994). The dashed box denotes the zonal band of high SSH variability of the STCC detected by the T/P altimeters.

Early theories on the STCC and the Subtropical Front by Roden (1975, 1980) and Welander (1981) have emphasized the Ekman convergence induced by westerlies to the north and trades to the south. More recent theories have stressed the importance of the surface buoyancy forcing coupled with the geostrophic convergence, which causes the midgyre front and its associated zonal current (Cushman-Roisin 1984; Kubokawa 1997). The numerical modeling studies by Takeuchi (1984, 1986) appear to support this geostrophic convergence theory. Dewar (1992), on the other hand, proposed that an *adiabatic* wind-driven model can cause such a surface front due to the nonlinear nature of the continuity equation.

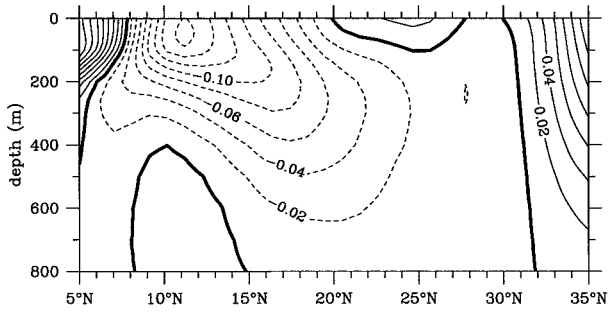

FIG. 3. Geostrophic zonal flow pattern along 145°E computed from the climatological temperature and salinity datasets of Levitus and Boyer (1994) and Levitus et al. (1994). The reference level is 1000 dbar and contour units are meters per second. The near-surface eastward flow between 19.5° and 27.5°N corresponds to the STCC.

Because the STCC encompasses a geographical domain as large as 60° in longitude (130°E–170°W) and 8° in latitude (19°–27°N), our knowledge about its spatial and temporal variability remains limited. With long-term observational data from the T/P satellite now available, this study attempts to first characterize the nature of the STCC variability. One interesting result revealed by the T/P altimeter data is that the mesoscale eddy field associated with the STCC–NEC system undergoes a remarkably regular seasonal cycle. In the second half of this study, a simple dynamic model is adopted to elucidate the causes of this seasonal eddy field modulation.

Another salient feature unveiled by Fig. 1 is that in the zonal band from 10°N to 18°N where the main body of the westward-flowing NEC is located, the SSH variability has relatively low rms values (<0.08 m). This result is somewhat unexpected given that the flow speed and the vertical velocity shear of the NEC are much stronger than those of the STCC. As shown in Fig. 3,

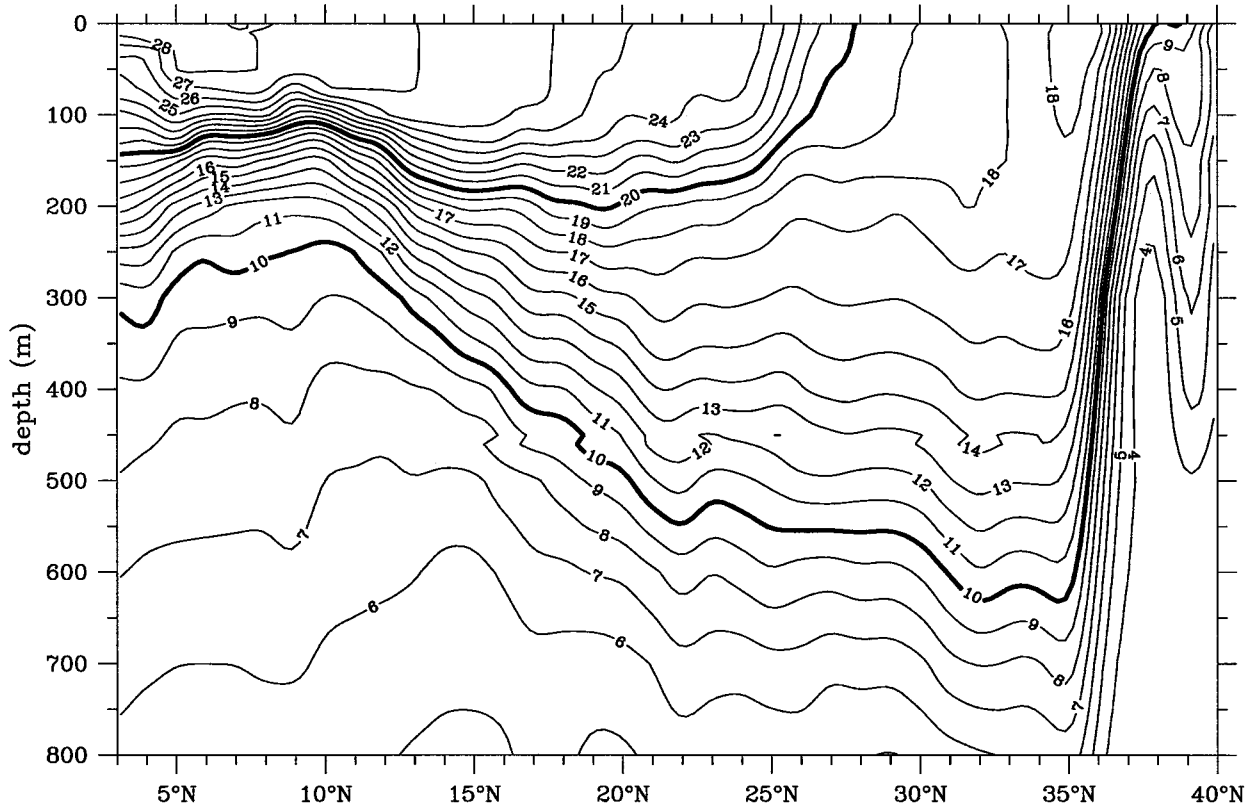

FIG. 4. Meridional temperature profile observed in the western North Pacific along 144°E in February 1987. Based on XBT and CTD measurements from R/V *Takuyo* of Japan Marine Safety Agency and R/V *Kaiyo-Maru* of Tohoku Regional Fisheries Research Laboratory.

the typical value for the NEC's vertical velocity shear is 3.5×10^{-4} s^{-1}, whereas it is 2.0×10^{-4} s^{-1} for the STCC. A recent study by Stammer (1997a) showed that the eddy kinetic energy level is closely related to the magnitude of the vertical shear in the mean flows: higher eddy variability regions coincide generally with stronger baroclinic mean flows. Clearly, the NEC and the STCC regions in the North Pacific Ocean do not follow this general tendency. In the present study, this observed aspect of the subtropical circulation variability will also be addressed.

This paper is organized as follows. In section 2, we start with a brief description of the T/P altimeter data and present results from the T/P data analysis. Particular attention is paid to the eddy kinetic energy field of the STCC and comparisons are made with other zonal currents in the North Pacific. In section 3, a vertically sheared 2½-layer reduced-gravity model is adopted to explore the physics underlying the observed seasonal modulation of the STCC eddy field. Discussions and stability properties of the NEC are provided in section 4. Section 5 summarizes the results from the present study.

2. Results from T/P altimeter data

TOPEX/Poseidon altimeter data from the period of October 1992 through December 1997 (repeat cycles 2–195) are used in this study. For all ground tracks passing the North Pacific Ocean, we first adjust the raw altimeter data for various environmental corrections, including the dry troposphere, the tides, and the inverse barometer effect, according to the GDR users handbook (Callahan 1993). After these corrections, the height data are interpolated to a common latitude grid with a one-per-second sample rate (about 5.6 km along a ground track). The alongtrack anomalous SSH profiles are then calculated by subtracting from each height profile the temporally averaged profile (namely, the geoid plus the 5¼-yr mean SSH). Finally, a low-pass filter, which has a half-power point at 26 km, is applied to the anomalous SSH data to suppress small-scale noises. Note that this low-pass filtering has little influence upon the mesoscale eddy signals of interest to this study.

Using the 5¼ yr of the T/P data, we plot in Fig. 5a the time series of the eddy kinetic energy averaged in the region of 19°–25°N, 135°E–175°W (i.e., the dashed box in Fig. 2). Here the eddy kinetic energy is estimated from the alongtrack anomalous SSH data (h') by assuming geostrophy and isotropic conditions, namely,

$$\text{EKE} \equiv \langle u_g^2 \rangle \quad \text{with } u_g = -\frac{g}{f}\frac{\partial h'}{\partial s}, \tag{1}$$

where u_g denotes the cross-track geostrophic velocity,

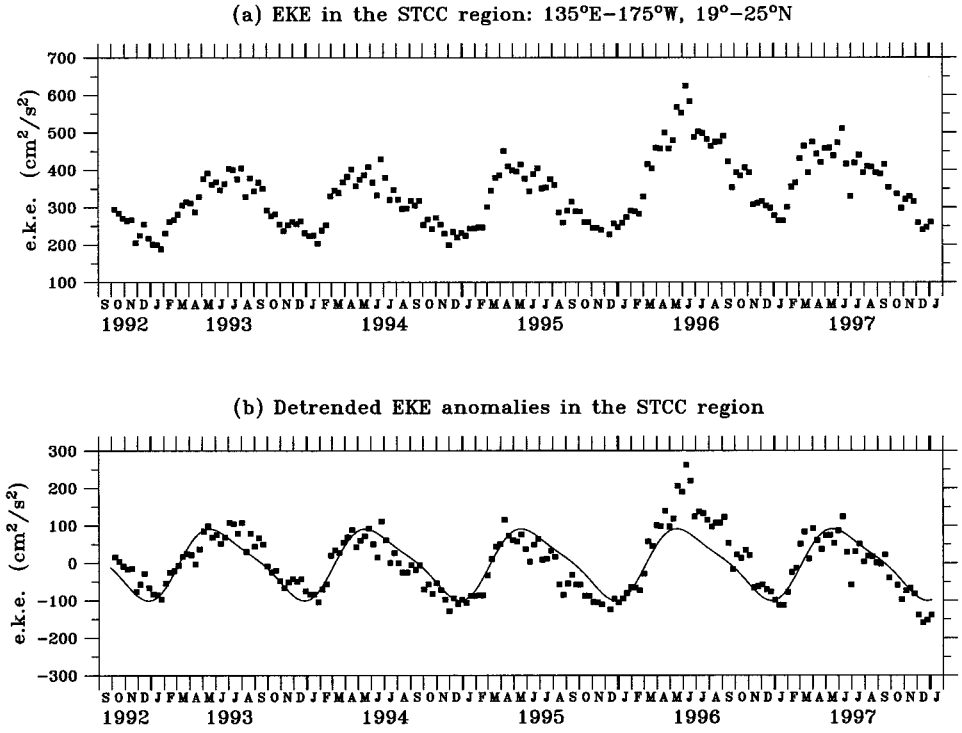

FIG. 5. (a) Time series of the eddy kinetic energy inferred from the T/P data in the STCC region 19°–25°N, 135°E–175°W. (b) Same as in (a) with linear trend removed. The solid line indicates the best fit by the annual and semiannual harmonics.

f is the Coliolis parameter, s is the alongtrack distance, and angle brackets denote the ensemble average from both the ascending and descending track estimates. The mean eddy kinetic energy level in the STCC region is 338 $cm^2\ s^{-2}$, which translates into a rms surface velocity change of 18 $cm\ s^{-1}$. Given that the mean flow of the STCC is 5 $cm\ s^{-1}$ or less,[1] this large rms surface velocity implies that the presence of the mean STCC can be masked by eddies for a given instance. This indeed is the case in some of the hydrographic data presented by Uda and Hasunuma (1969) and Hasunuma and Yoshida (1978) in which the eastward-flowing STCC is often ''blurred'' by signals of mesoscale eddies.

One interesting result revealed by Fig. 5a is the existence of a distinct annual cycle in the STCC's eddy kinetic energy field; the EKE level of the STCC attains a maximum in April/May and decreases to a minimum in December/January. This seasonal eddy field modulation becomes even clearer if we remove the linear trend in Fig. 5a and fit a curve with the annual and semiannual harmonics (see Fig. 5b). The amplitude of the seasonal eddy kinetic energy change is large: the EKE level in April/May (~440 $cm^2\ s^{-2}$) is double that of December/January. Figure 6 shows the zonally averaged EKE distributions as a function of season and latitude. Notice that the meridional EKE profiles do not depend sensitively on the season: the EKE peak, for example, is located around 22°N in all seasons. In spring (AMJ), a secondary EKE peak can be found around 19°N, although its presence is less clear in the other seasons.

To highlight the regularity in the EKE field of the STCC, we plot in Fig. 7 the eddy kinetic energy time

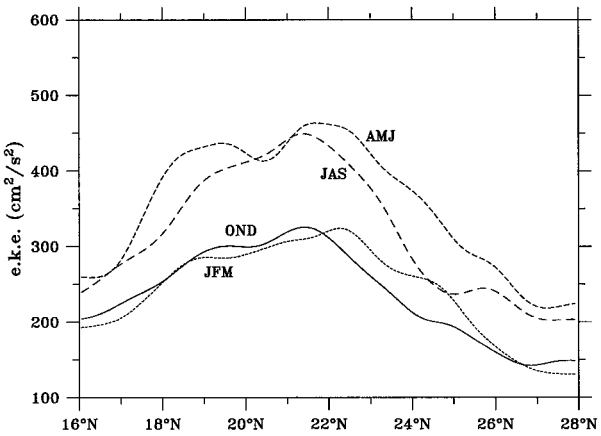

FIG. 6. Meridional profiles of the zonally averaged eddy kinetic energy distributions (135°E–175°W) in the four seasons, JFM: winter; AMJ: spring; JAS: summer; and OND: fall.

[1] The mean kinetic energy level in the region of 19°–25°N, 135°E–175°W based on the climatological surface geostrophic flow is 1.9 $cm^2\ s^{-2}$.

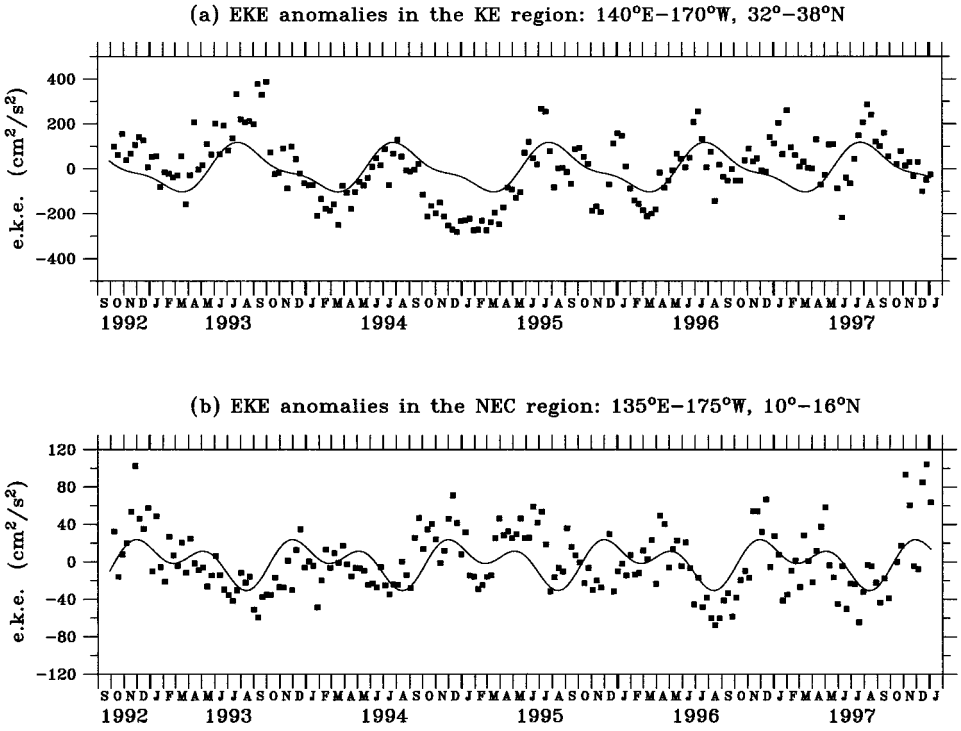

FIG. 7. (a) Time series of the eddy kinetic energy (with the linear trend removed) in the Kuroshio Extension region 32°–38°N, 140°E–170°W. (b) Same as (a) except for the NEC region 10°–16°N, 135°E–175°W. The solid line in each panel indicates the best fit by the annual and semiannual harmonics.

series in its two neighboring current regions: the Kuroshio Extension (32°–38°N, 140°E–170°W) and the NEC (10°–16°N, 135°E–175°W). Like in Fig. 5b, these time series have been detrended and their mean EKE and linear trend values are summarized in Table 1. For both the Kuroshio Extension and the NEC, the seasonal EKE signals are much less prominent. The annual/semiannual harmonic curves in both Figs. 7a and 7b explain less than 25% of the variances in the detrended EKE time series. This is in sharp contrast to the annual/semiannual harmonic curve in Fig. 5b, which explained 70% of the EKE variance in the STCC.

Figure 5 shows that the interannual variations exist in the eddy field of the STCC as well. The EKE level, for example, is unseasonably high in March–October 1996. In addition, a linear trend with an annual EKE increase of 23 $cm^2\ s^{-2}$ is present in the time series shown in Fig. 5a. Over the 5¼-yr period of the T/P mission, this amounts to an EKE increase of 120 $cm^2\ s^{-2}$, or a 35% increase over the mean EKE level of the STCC. Interestingly, a long-term increase in the EKE level with a similar ratio (29%; see Table 1) is also observed in the NEC during the same period. In contrast, the eddy kinetic energy level in the Kuroshio Extension experienced a weak drop over the 5¼ yr of the T/P mission (see also Qiu 1995). Though important, the details of the interannual changes in these current systems will not be pursued in this study.

It is worth emphasizing that the seasonal eddy field modulation detected by the T/P altimeters is not a result of the seasonal steric height change (Stammer 1997b) or of the changes due to the seasonal migration and intensification of the STCC. To explicitly evaluate the EKE changes due to these factors, we calculated the EKE time series based on the low-pass filtered anomalous SSH data. The low-pass filter adopted has a half-pass point at 300 days and effectively removes the intraannual, mesoscale signals. The EKE changes thus computed have a peak-to-peak seasonal amplitude of less than 20 $cm^2\ s^{-2}$, much smaller than the seasonal amplitude of 200 $cm^2\ s^{-2}$ shown in Fig. 5. In other words, the eddy kinetic energy signals in Fig. 5 are mostly associated with the eddy field of the STCC as opposed to the seasonal changes of the mean STCC itself.

TABLE 1. The mean eddy kinetic energy level, the linear trend in the EKE field over the 5.2 years of the T/P mission, and the ratio of the long-term EKE change over the mean EKE value in the zonal current regions of the STCC, the Kuroshio Extension, and the NEC.

Current	Mean EKE level ($cm^2\ s^{-2}$)	Linear trend ($cm^2\ s^{-2}\ yr^{-1}$)	Ratio of long-term EKE change
STCC	338	22.9	35.2%
Kuroshio Extension	661	−19.4	−15.3%
NEC	217	12.0	28.8%

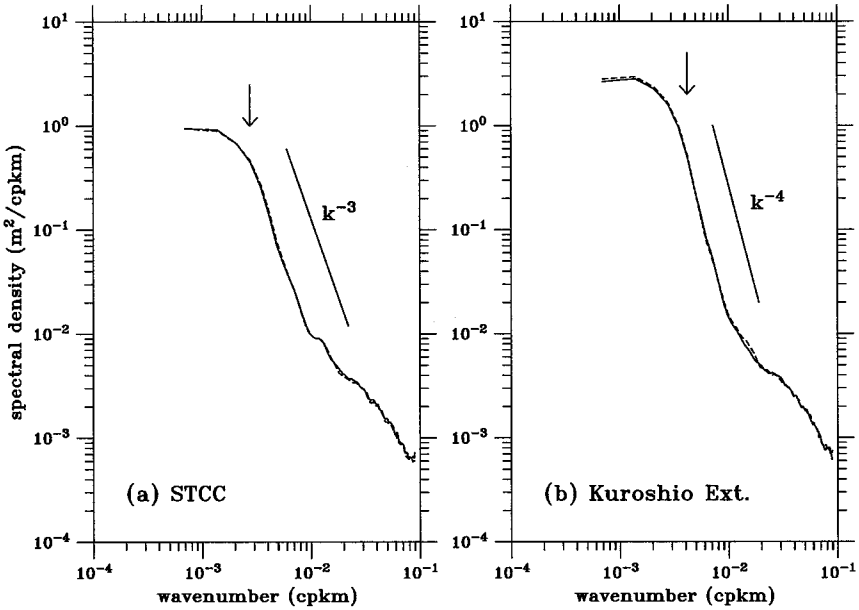

FIG. 8. Wavenumber spectra of the along-track SSH averaged in (a) the STCC region (18°–30°N, 135°E–175°W) and (b) the Kuroshio Extension region (29°–41°N, 140°E–170°W). Solid lines denote the spectra estimated from the ascending track data and dashed lines from the descending track data. Arrows denote the scale of 2π times the first-mode Rossby radius of deformation. Unfiltered T/P data of 1993 and 1994 (repeat cycles 11–83) are used for both (a) and (b).

To examine the length scale of the eddy field in detail, we estimated the mean wavenumber spectra of the alongtrack SSH data in the region 18°–30°N, 135°E–175°W (Fig. 8a). Here a meridional segment of 12° is chosen in order to estimate the spectral distribution at wavelengths longer than the first-mode Rossby radius of deformation. Notice that the spectra derived independently from the ascending and descending track data are nearly identical. In the intermediate wavelengths (100–300 km), Fig. 8a shows that the spectra are well represented by a k^{-3} dependence, with k being the alongtrack wavenumber. As the wavelengths become longer than 350 km, the spectra begin to level off. As noted by several previous studies (e.g., Fu 1983; Le Traon et al. 1990; Stammer 1997a), this break in the spectral slope occurs close to 2π times the regional first-mode Rossby radius of deformation, and separates the geostrophic turbulent regime from the regime where the planetary β effect dominates. From Emery et al. (1984) and Chelton et al. (1998), the first-mode Rossby radius of deformation R_{oi} in the STCC is about 58 km, or $2\pi R_{oi}$ = 364 km (see the arrow in Fig. 8a). Because the first-mode Rossby radius of deformation is the preferred length scale for eddies generated by the process of baroclinic instability (Pedlosky 1987), the result of Fig. 8a hints that such an instability process is likely at work in the STCC system. This hypothesis will be tested in the following section.

In concluding this section, we show in Fig. 8b the mean wavenumber spectra in the Kuroshio Extension region estimated from the T/P altimeter data. In this region of higher eddy kinetic energy, the spectral slope in the intermediate wavelength range follows k^{-4}, steeper than that in the STCC region. As in the STCC region, however, the spectral break occurs again near 2π times the regional first-mode Rossby radius of deformation. The averaged R_{oi} in the Kuroshio Extension region is about 38 km (Emery et al. 1984; Chelton et al. 1998). In both Figs. 8a and 8b, a $k^{-1.5}$ relation is found for signals with wavelengths shorter than 100 km; this appears to be a global feature of the T/P data and is attributable to the ''noises'' due to environmental and geophysical corrections (Stammer 1997a).

3. Theoretical considerations

That the spectral regime shift occurs around $2\pi R_{oi}$, as revealed above from the T/P data analysis, suggests that the eddy field of the STCC is possibly related to the baroclinic instability process. This, in turn, points to the importance of the vertical velocity shear between the eastward-flowing STCC and the westward-flowing NEC. Given the shallow presence of the STCC, it is of no surprise that the vertical velocity shear between the STCC and its underlying NEC is sensitive to the seasonal surface wind and buoyancy forcings. In Fig. 9, we present the thermal structures and the zonal geostrophic velocity profiles of the STCC–NEC in the four months representing different seasons. Due to the surface cooling beginning in late October, the well-strati-

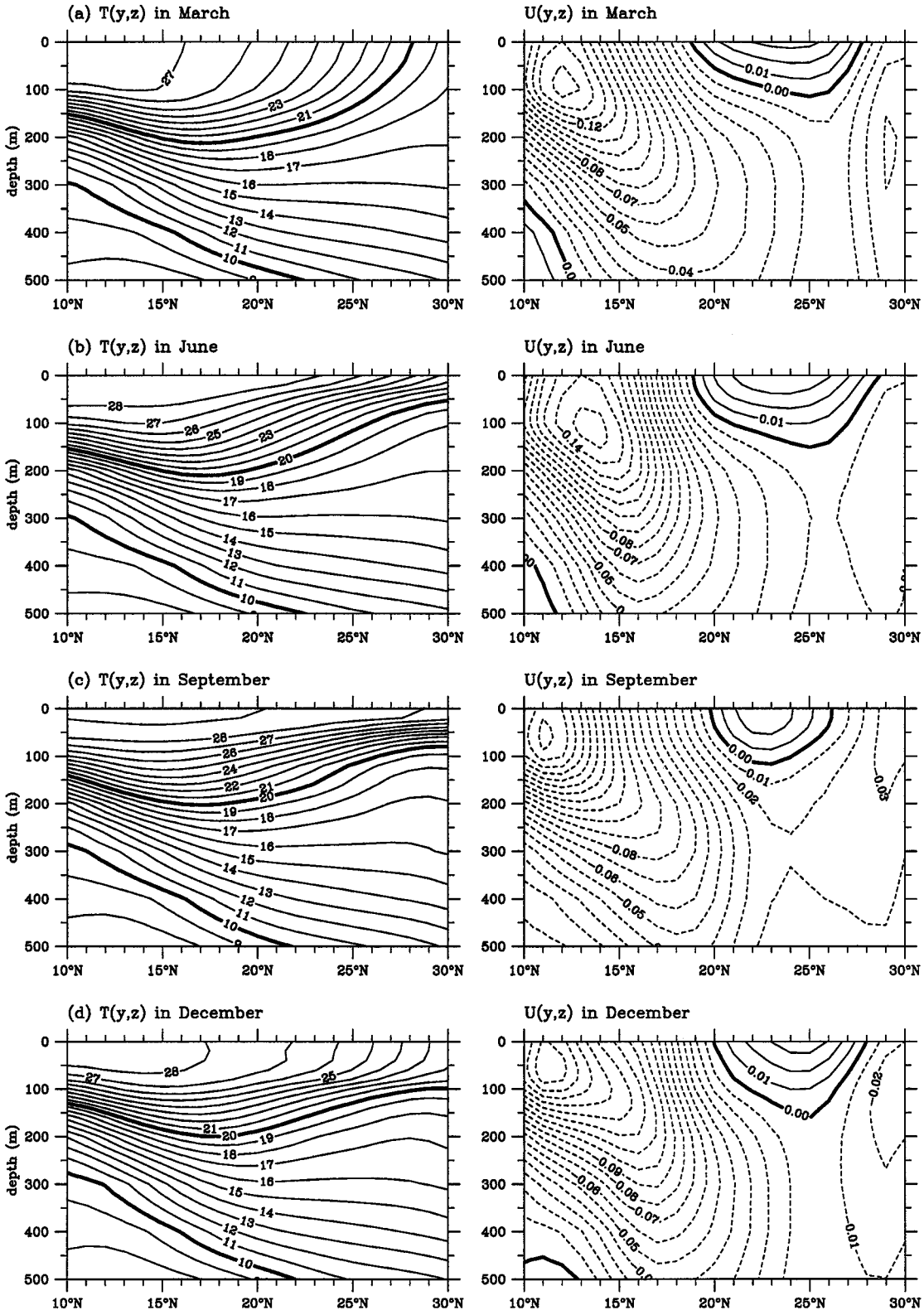

FIG. 9. Seasonal evolution of the thermal structures and the zonal geostrophic velocities of the STCC and the NEC along 150°E. Based on the monthly climatological *T–S* datasets of Levitus and Boyer (1994) and Levitus et al. (1994). Contour units are degrees Celsius for temperature and meters per second for velocity. The reference level is 1000 dbar.

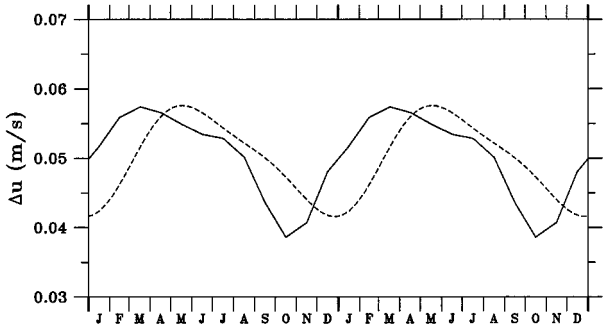

FIG. 10. Seasonal change in the vertical velocity shear between the STCC and its underlying NEC (solid line) vs the seasonal change in the detrended EKE level of the STCC from the T/P observations (dashed line; same as the solid line in Fig. 5b). Here, the vertical velocity shear is the climatological, zonal velocity shear between 0 and 400 m averaged in the region of 19°–25°N, 140°–170°E. Based on the monthly *T–S* datasets of Levitus and Boyer (1994) and Levitus et al. (1994).

fied upper thermocline of the STCC of summer/fall (Fig. 9c) is destroyed in winter (Fig. 9d). As the latitudinally varying surface cooling progresses, the convectively induced tilt of the upper thermocline enhances and it reaches the maximum in early spring (Fig. 9a). The steep thermal front structure of the STCC is subsequently replaced by a flatter seasonal thermocline when the surface buoyancy forcing changes from cooling to heating (Fig. 9b).

The dynamical consequence of this seasonal upper-thermocline evolution is that the vertically sheared STCC–NEC system undergoes a regular seasonal change. The vertical velocity shear of the STCC–NEC, as shown in Fig. 10 (solid line), is strongest in March when the upper-thermocline tilt reaches the maximum and is weakest in October when the stratified seasonal thermocline starts to collapse. Notice that the peak-to-peak amplitude of this seasonal change, 0.02 m s^{-1}, is 40% that of the mean vertical shear between the STCC and the NEC (0.05 m s^{-1}). Because of the nature of the mixed layer dynamics (e.g., Denman 1973), the annual cycle of the vertical STCC–NEC shear is asymmetric, with the wintertime increase in velocity shear taking place at a faster rate than the weakening of the shear over the summer and fall seasons. It is interesting to note that the annual cycle of the STCC–NEC shear leads the eddy kinetic energy cycle of the STCC (the dashed line in Fig. 10) by about 2 months. A hypothesis that we can form based on Fig. 10 is that as the vertical shear intensifies in late winter and early spring, the STCC–NEC becomes baroclinically unstable, and this instability weakens when the vertical velocity shear of the STCC–NEC decreases in the summer and fall seasons. In other words, the distinct annual cycle in the eddy kinetic energy level of the STCC region is a manifestation of the intensity of the baroclinic instability and that the 2-month lag is the length of time the unstable waves need to fully grow.

To test this hypothesis, we adopt in this study a simple dynamic model in which the ocean is assumed to consist of two active upper layers and an infinitely deep abyssal layer (a.k.a., the 2½-layer reduced-gravity model). In the surface layer, we assume the mean layer thickness is H_1 and the mean zonal flow is U_1, representing the eastward-flowing STCC. In the second layer, the mean layer thickness is H_2 and the mean zonal flow is U_2, which corresponds to the westward-flowing NEC. The density in each layer is assumed to be ρ_n ($n = 1$, 2, and 3). Under the quasigeostrophic approximation, the linearized equations governing the perturbation potential vorticity q_n are

$$\left(\frac{\partial}{\partial t} + U_n\frac{\partial}{\partial x}\right)q_n + \frac{\partial \Pi_n}{\partial y}\frac{\partial \phi_n}{\partial x} = 0, \tag{2}$$

where ϕ_n is the perturbation streamfunction and Π_n is the mean potential vorticity in the n layer ($n = 1$ and 2; see Pedlosky 1987).

For simplicity, we will assume that the mean flow U_n are meridionally uniform. This assumption eliminates the barotropic instability mechanism from our consideration. Justifications for this assumption will be considered in section 4a. Given the constant U_n, the perturbation streamfunction and the meridional gradient of Π_n in the 2½-layer reduced-gravity model can be expressed by

$$q_1 = \nabla^2\phi_1 + \frac{1}{\gamma\delta\lambda^2}(\phi_2 - \phi_1) \tag{3}$$

$$q_2 = \nabla^2\phi_2 + \frac{1}{\gamma\lambda^2}(\phi_1 - \phi_2 - \gamma\phi_2) \tag{4}$$

$$\Pi_{1y} = \beta + \frac{1}{\gamma\delta\lambda^2}(U_1 - U_2) \tag{5}$$

$$\Pi_{2y} = \beta - \frac{1}{\gamma\lambda^2}(U_1 - U_2 - \gamma U_2), \tag{6}$$

where

$$\delta \equiv \frac{H_1}{H_2}, \qquad \gamma \equiv \frac{\rho_2 - \rho_1}{\rho_3 - \rho_2}, \quad \text{and}$$

$$\lambda \equiv \frac{1}{f_o}\sqrt{\frac{(\rho_3 - \rho_2)}{\rho_o}gH_2}. \tag{7}$$

In the above equations, ∇^2 denotes the horizontal Laplacian operator, β the meridional gradient of the Coriolis parameter, f_o the Coriolis parameter at the reference latitude, and ρ_o the reference density. In Eq. (7), δ is the layer depth ratio and γ is the stratification ratio. The reason that we have chosen the internal Rossby radius λ to be scaled by the second-layer quantities, that is, H_2 and $\rho_3 - \rho_2$, in Eq. (7) will become obvious in the following discussion.

By substituting the normal mode solution

$$\phi_n = \mathrm{Re}[A_n \exp i(kx + ly - kct)] \tag{8}$$

TABLE 2. Parameter values appropriate for the STCC–NEC system in the spring and fall seasons. Dashes in the third column denote the fall value the same as that in the spring season.

Parameter	Spring value	Fall value
f_o	5.23×10^{-5} s^{-1}	—
β	2.15×10^{-11} s^{-1} m^{-1}	—
U_1	0.03 m s^{-1}	0.01 m s^{-1}
U_2	−0.03 m s^{-1}	—
H_1	150 m	—
H_2	300 m	—
ρ_1	23.90 σ_θ	22.85 σ_θ
ρ_2	26.00 σ_θ	—
ρ_3	27.75 σ_θ	—
γ	1.2	1.8
$2\pi/l$	300 km	—

into Eq. (2) and using Eqs. (3)–(6), we have

$$(U_1 - c)\left[-K^2A_1 + \frac{1}{\gamma\delta\lambda^2}(A_2 - A_1)\right] + \Pi_{1y}A_1 = 0 \quad (9)$$

$$(U_2 - c)\left[-K^2A_2 + \frac{1}{\gamma\lambda^2}(A_1 - A_2 - \gamma A_2)\right] + \Pi_{2y}A_2 = 0, \quad (10)$$

where $K^2 \equiv k^2 + l^2$ is the total wavenumber. Requiring nontrivial solutions for A_n leads to

$$c^2 - \left(U_1 + U_2 - \frac{P + Q}{R}\right)c + \left(U_1U_2 + \frac{\Pi_{1y}\Pi_{2y}}{R} - \frac{U_1P}{R} - \frac{U_2Q}{R}\right) = 0, \quad (11)$$

where

$$P = \left(K^2 + \frac{1}{\gamma\delta\lambda^2}\right)\Pi_{2y}, \qquad Q = \left(K^2 + \frac{1 + \gamma}{\gamma\lambda^2}\right)\Pi_{1y},$$

and

$$R = \left(K^2 + \frac{1 + \gamma}{\gamma\lambda^2}\right)\left(K^2 + \frac{1}{\gamma\delta\lambda^2}\right) - \frac{1}{\gamma^2\delta\lambda^4}. \quad (12)$$

Notice that the results of the above 2½-layer reduced-gravity model reduce to those of the Phillips two-layer model if we take $\gamma \to 0$ and $\gamma\lambda^2 \to (\rho_2 - \rho_1)gH_2/\rho_o f_o^2$ [see Pedlosky (1987) for details]. The 2½-layer reduced-gravity model has also been used recently by Liu (1999) to examine the behaviors of baroclinic Rossby waves in the main thermocline in the planetary wave limit (i.e., $K \to 0$).

In Table 2, we summarize the parameter values appropriate for the STCC–NEC system in the spring and fall seasons, respectively. The reference latitude for f_o and β is taken at 21°N; the other parameter values are estimated from the monthly, climatological datasets of Levitus and Boyer (1994) and Levitus et al. (1994). The

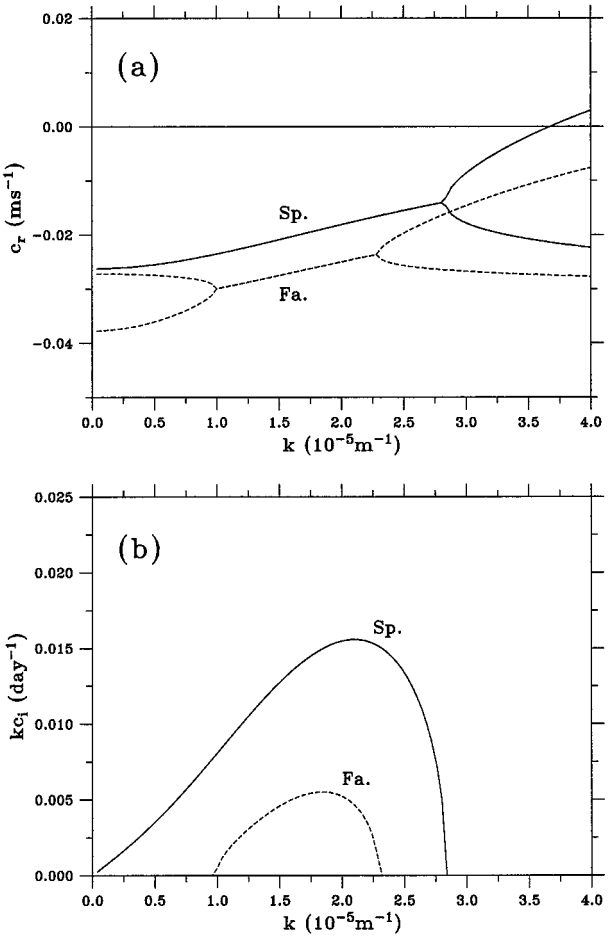

FIG. 11. (a) Phase speed and (b) growth rate as a function of zonal wavenumber k calculated from Eq. (11). Solid lines are the results for spring and dashed lines for fall. Parameter values appropriate for the spring and fall seasons are given in Table 2.

major difference between the spring and fall conditions resides in two parameters: U_1 and γ. While the springtime STCC (or U_1) is relatively fast, its speed is reduced in fall due to the flattening of the upper thermocline. As shown in Fig. 10, the reduction in U_1 in the fall season is about 0.02 m s^{-1}. The stratification ratio γ [recall Eq. (7)] for the STCC–NEC is about 1.2 in the spring season; it increases to 1.8 in fall due to the surface heating, which decreases the surface layer density ρ_1 (see Fig. 9). Notice that in the second layer, the thermal structure and the flow condition of the NEC are relatively stable regardless of the season.

Using Eq. (11) with $c \equiv c_r + ic_i$ and the values listed in Table 2, we plot in Fig. 11 the phase speed (c_r) and the growth rate (kc_i) of the STCC–NEC system as a function of the zonal wavenumber k. The solid and dashed lines denote the results under the spring and fall conditions, respectively. Although the STCC–NEC system is unstable under both conditions, a substantial difference in the growth rate is found between the two

seasons. The most unstable wave in spring has $kc_i = 0.0156$ day^{-1}, or an e-folding timescale of 64 days, whereas the e-folding timescale under the fall condition is O(180 days). In addition, the window within which the unstable waves are permissible is considerably narrower in fall than in spring (Fig. 11b). Notice that the difference between the two seasons also appears in the phase speed for the most unstable mode: in spring, $c_r = -1.8$ cm s^{-1}, whereas it is -2.6 cm s^{-1} in fall.

The result that the springtime STCC–NEC system is baroclinically more unstable than its fall counterpart is attributable to the stronger vertical shear $U_1 - U_2$ and the reduced stratification ratio (i.e., a smaller γ) of the spring season. Physically this can be understood in terms of the stability criterion for the 2½-layer reduced-gravity system. Multiplying Eq. (9) by $A_1H_1/(U_1 - c)$ and Eq. (10) by $A_2H_2/(U_2 - c)$ and adding the two results, we have

$$K^2(H_1A_1^2 + H_2A_2^2) + \frac{H_2}{\gamma\lambda^2}(A_1 - A_2)^2 + \frac{H_2}{\lambda^2}A_2^2 = \frac{H_1\Pi_{1y}}{U_1 - c}A_1^2 + \frac{H_2\Pi_{2y}}{U_2 - c}A_2^2. \quad (13)$$

As both the real and imaginary part of Eq. (13) must vanish separately, we have

$$c_i\left(\frac{H_1\Pi_{1y}}{|U_1 - c|^2}A_1^2 + \frac{H_2\Pi_{2y}}{|U_2 - c|^2}A_2^2\right) = 0 \quad (14)$$

from the imaginary part. For the mode to be unstable ($c_i \neq 0$), Eq. (14) indicates

$$\Pi_{1y}\Pi_{2y} < 0; \quad (15)$$

namely, the potential vorticity gradient of the mean state in the two active layers must be opposite. Since $U_1 - U_2 > 0$ in the STCC–NEC system, Π_{1y} is always positive [recall Eq. (5)]. As such, the necessary condition for instability of the modeled STCC–NEC system is $\Pi_{2y} < 0$. By rewriting Eq. (6), this leads to

$$U_1 - (1 + \gamma)U_2 > \gamma\lambda^2\beta. \quad (16)$$

Clearly, a stronger vertical velocity shear $U_1 - U_2$ and a smaller stratification ratio γ would help meet this condition and thereby increase the potential for the baroclinic instability.

4. Discussions

The stability analysis result presented above supports the notion that the well-defined annual cycle in the eddy kinetic energy field of the STCC region reflects the seasonal modulation in intensity of the baroclinic instability of the STCC–NEC system. The two important factors controlling this seasonal modulation are the flow speed of the STCC and the density in the STCC layer; the former determines the vertical velocity shear and the latter influences the stratification of the seasonally varying basic state.

a. Presence of the Subtropical Front

The adoption of a 2½-layer, reduced-gravity model in section 3 precludes the dynamics associated with the surfacing of the Subtropical Front, such as the barotropic and frontal instabilities. The effect of the Subtropical Front, which appears in winter/spring along 26°N (see Fig. 4), is not pursued in this study for the following reasons. The high EKE band, as shown in Fig. 6, exists *south* of 25°N. That the EKE peak in all seasons is located around 22°N suggests that the energy source for the observed high EKE does not reside in the Subtropical Front. A careful look at the zonal velocity profiles in Fig. 9 indicates that the high EKE band of 19°–25°N is where the westward-flowing NEC beneath the STCC is relatively strong. Beneath the Subtropical Front in winter and spring, Fig. 9 shows the westward flow being close to zero. This fact points to the importance of the vertical velocity shear between the NEC and STCC in providing the energy source for the observed eddy field. It also justifies the use of the 2½-layer, reduced-gravity model for understanding the instability processes in the STCC–NEC system.

b. Parameter sensitivity of the STCC–NEC system

In this subsection, we will comment on some of the parameter values listed in Table 2 and discuss the instability sensitivity of the various basic-state parameters. From the thermal-wind relation and the climatological temperature–salinity data, we are able to obtain a reliable time series of the vertical velocity shear between the STCC and the NEC, $U_1 - U_2$ (Fig. 10). The values for U_1 and U_2, however, can be offset by a reference mean flow (defined below as U_b) because of the assumption of a level of no-motion. The magnitude of this mean flow may be estimated from the ocean general circulation model (OGCM) that is driven by realistic surface wind and buoyancy fluxes. In the OGCM result presented by Semtner and Chervin (1992, their Fig. 12), the depth-averaged transport in the STCC region is about 3 Sv/° lat (Sv $\equiv 10^6$ m^3 s^{-1}) westward. With an average depth of 3000 m in the region, this translates into a zonal mean flow of $U_b = -0.9$ cm s^{-1}. In Fig. 12a, we plot the growth rate dependence on U_b, when it is varied in the range of ± 4.0 cm s^{-1} under the springtime condition of the STCC–NEC. (The solid line of Fig. 11b corresponds to the section along $U_b = 0$ in Fig. 12a.) While the addition of a mean zonal flow in the two active upper layers does change the instability characteristics, its effect is quantitatively small when U_b is on the order of 1 cm s^{-1}.

It is interesting to note from Fig. 12a that a westward mean flow ($U_b < 0$) works to enhance the baroclinic instability, whereas an eastward U_b tends to weaken the instability. This again can be understood by the stability criterion derived in section 3. With an addition of U_b

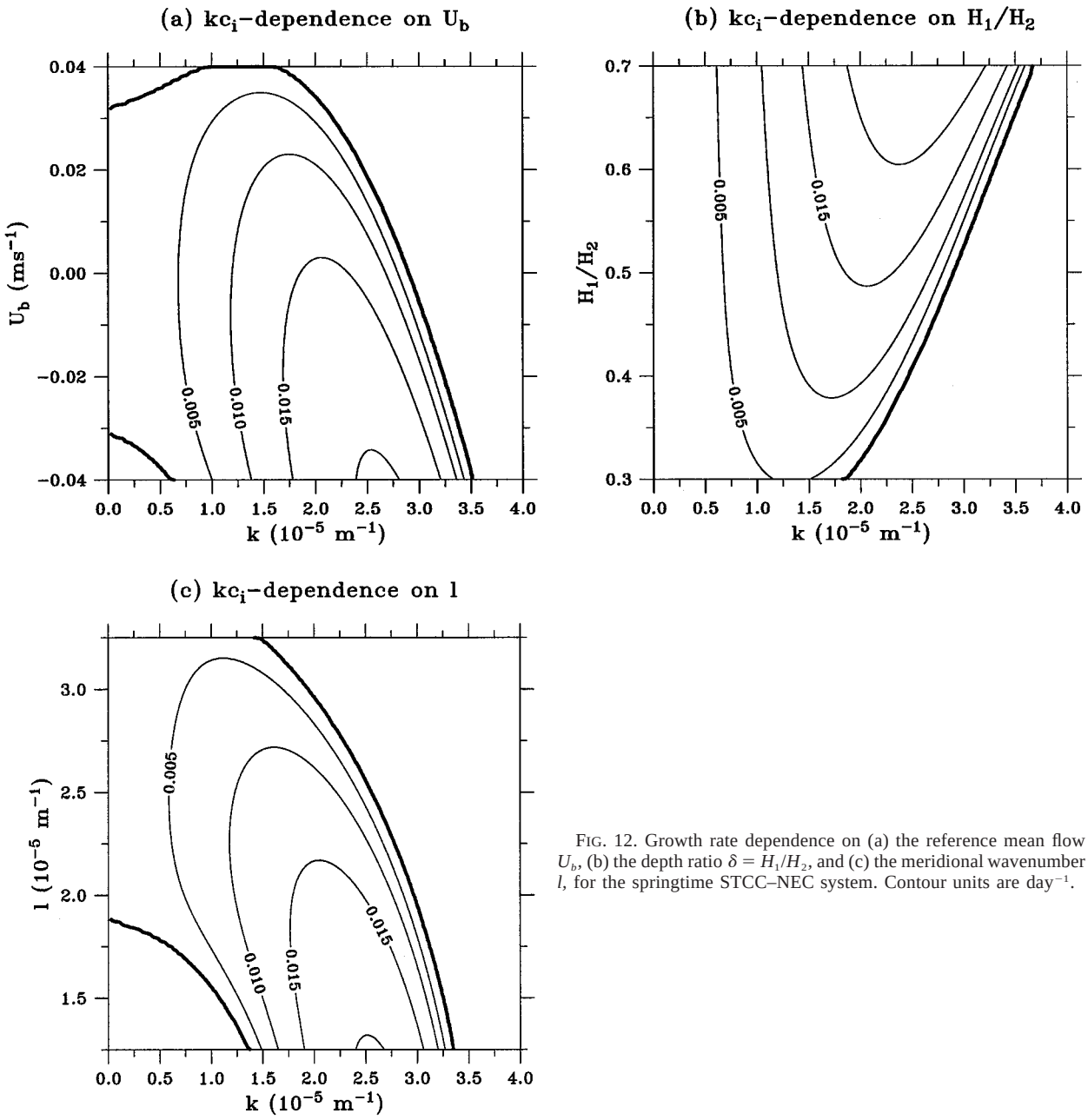

FIG. 12. Growth rate dependence on (a) the reference mean flow U_b, (b) the depth ratio $\delta = H_1/H_2$, and (c) the meridional wavenumber l, for the springtime STCC–NEC system. Contour units are day^{-1}.

to U_1 and U_2, the necessary condition for instability, Eq. (16), modifies to

$$U_1 - (1 + \gamma)U_2 - \gamma U_b > \gamma\lambda^2\beta. \qquad (17)$$

As the density ratio γ is a positively defined quantity, an eastward U_b would reduce the potential for the baroclinic instability, whereas a westward U_b would enhance such a potential.

The values of H_n and ρ_n in Table 2 determine the two nondimensional parameters δ and γ as defined in Eq. (7). For the H_n values listed in Table 2, we selected the mean depth above the 24.8 σ_θ density surface as H_1 and the mean layer thickness between the 24.8 σ_θ and 26.2 σ_θ density surfaces as H_2. These two density surfaces correspond roughly to the 20° and 12°C isotherms in Fig. 9, respectively. The Levitus climatological *T–S* data were then used to determine ρ_n in the individual layers. Figure 12b shows the growth rate as a function of k when H_2 is selected differently under the springtime condition. Note that changing H_2 also affects the ρ_2 value, and this adjustment based on the climatological *T–S* data is incorporated in Fig. 12b. (The solid line of Fig. 11b corresponds to the section along $\delta = 0.5$ in Fig. 12b.) As in Fig. 12a, a different H_1/H_2 ratio changes

the stability characteristics quantitatively. In particular, a larger H_2 value moves the short-wave cutoff to a longer wavelength whereas a smaller H_2 value (i.e., as H_2 becomes more comparable to H_1) expands the window for the permissible unstable waves. This dependence on H_2 can again be explained by Eq. (16) with the recognition that λ^2 on the rhs of Eq. (16) is proportional to H_2.

The last parameter $2\pi/l$ in Table 2 is the meridional wavelength assumed in the normal mode solution. Its value, 300 km, is chosen such that the zonal wavelength of the resultant most unstable mode has a comparable scale (i.e., the eddy field is nearly isotropic), as suggested by the T/P altimeter measurement. Figure 12c shows the growth rate dependence when l is altered in the range between $2\pi/l = 193$ km and 500 km for the springtime STCC–NEC system. (The solid line of Fig. 11b corresponds to the section along $l = 2.09 \times 10^{-5}$ m^{-1} in Fig. 12c.) As the assumed l value increases, the zonal wavenumber k of the most unstable mode decreases, and vice versa. In the real ocean, l is a quantity to be determined *by* the baroclinic instability process, rather than prescribed. If the isotropic assumption is valid, Fig. 12c indicates that the most unstable mode with $k = l$ should have a length scale of 300 km. Notice that this scale is close to where the spectral slope inferred from the T/P data changes from the geostrophic turbulent region to the β-dominant regime (Fig. 8a).

c. Stability of the NEC

In contrast to the STCC–NEC system in the zonal band of 19°–25°N, the T/P result further revealed that the westward-flowing NEC in the zonal band of 10°–18°N is comparatively stable (Fig. 1). As may be easily identified in Fig. 3, this band corresponds to the main body of the NEC that has a fast surface velocity core of 0.16 m s^{-1} with a substantial vertical velocity shear above the main thermocline. Why is this stronger zonal current less eddy energetic than its neighboring, weakly sheared STCC–NEC system?

Insight for answering this question can again be gained from the simple 2½-layer model of section 3. By dividing the upper ocean above the main thermocline into two sublayers, we list in Table 3 the parameter values appropriate for the NEC under the 2½-layer representation. Like for the STCC–NEC system, the parameter values were chosen based on the Levitus climatological *T–S* data. For these values, the solution to Eq. (11) indicates that the NEC is baroclinically *stable*. In fact, when the maximum growth rate is plotted as a function of U_1 and U_2 for the parameter values listed in Table 3, Fig. 13 shows that a westward-flowing current with $|U_1| > |U_2|$ (i.e., the upper-left half of the third quadrant in Fig. 13) is mostly stable.

To understand this result, it is helpful to reexamine the necessary condition for instability, Eq. (15). Unlike the STCC–NEC system, the potential vorticity gradient of the second layer, Π_{2y}, for a westward-flowing current such as the NEC will be positive [see the definition in Eq.(6)]. In order to satisfy Eq. (15) in this case, the upper-layer potential vorticity gradient Π_{1y} must be negative, or,

$$|U_1 - U_2| > \delta\gamma\lambda^2\beta. \tag{18}$$

The rhs of Eq. (18) may be rewritten as $\beta g H_1(\rho_2 - \rho_1)/\rho_o f_o^2$ and is a measure of the baroclinic Rossby wave speed. For the values appropriate for the NEC (Table 3), $\delta\gamma\lambda^2\beta = 0.096$ m s^{-1}. Thus, the vertical velocity shear has to be at least 0.096 m s^{-1} in order for the NEC to become baroclinically unstable. Notice that Eq. (18) is not a *sufficient* condition for the baroclinic instability.[2] In fact, there exists a large area in the U_1/U_2 space of Fig. 13 where a westward flow is stable even though its vertical velocity shear $|U_1 - U_2|$ exceeds 0.096 m s^{-1} (see the stippled area in Fig. 13). The NEC with $U_1 = -0.15$ m s^{-1} and $U_2 = -0.05$ m s^{-1} falls in this area. One important factor contributing to the NEC's stability is its presence in low latitude. As shown in Fig. 2, the center latitude for the NEC in the western North Pacific is along 13°N. Being in a low latitude increases the in situ baroclinic Rossby wave speed $\delta\gamma\lambda^2\beta$ and raises the minimum vertical velocity shear required for the NEC to be baroclinically unstable. Were it located in the latitude band of the STCC, the NEC would have been baroclinically unstable.

Admittedly, a layered model with only two active layers tends to suppress the weaker instability modes that would otherwise exist in a continuously stratified model (Pedlosky 1987). The result that for zonal currents above the main thermocline, a westward flow with $\partial U/\partial z < 0$ would be baroclinically more stable than a surface-eastward/subsurface-westward flow is a robust feature. This is so because the same potential vorticity argument for the 2½-layer reduced-gravity model is valid for a more complicated model of the NEC. This feature, together with the fact that the NEC is located at a

TABLE 3. Parameter values appropriate for the 2½-layer reduced-gravity NEC model.

Parameter	NEC
f_o	3.28×10^{-5} s^{-1}
β	2.24×10^{-11} s^{-1} m^{-1}
U_1	-0.15 m s^{-1}
U_2	-0.05 m s^{-1}
H_1	150 m
H_2	150 m
ρ_1	22.85 σ_θ
ρ_2	26.00 σ_θ
ρ_3	27.75 σ_θ
γ	1.8
$2\pi/l$	330 km

[2] The sufficient condition in this case is that the discriminant of Eq. (11) is negative.

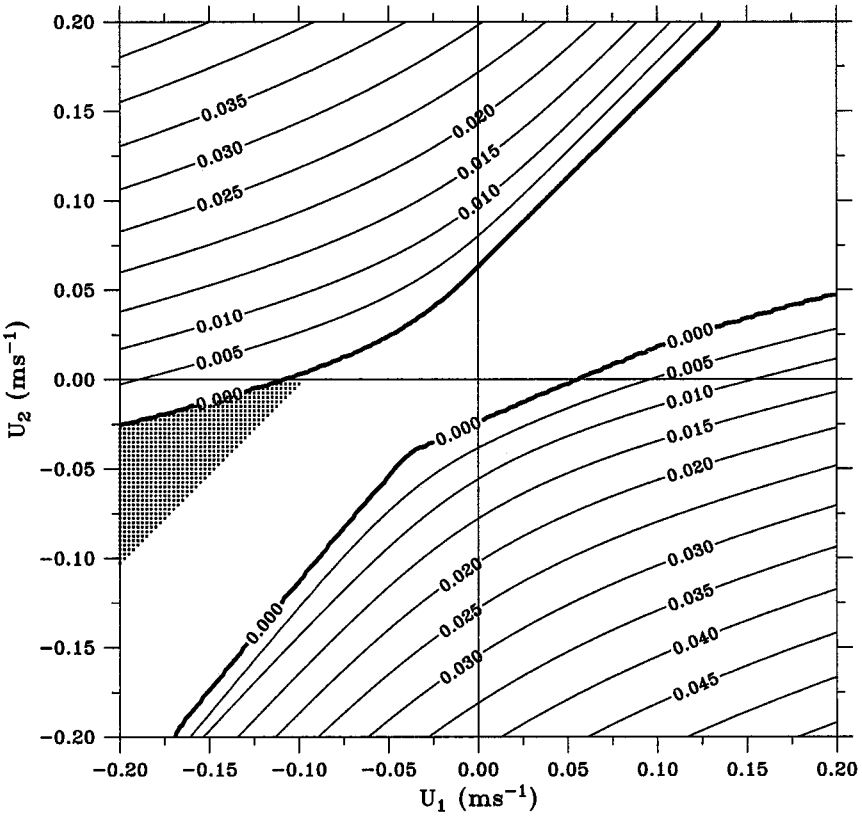

FIG. 13. Maximum growth rate dependence on U_1 and U_2 in the 2½-layer NEC model (see Table 3 for the parameters). The region between the two thick lines are dynamically stable. The stippled region in the third quadrant ($U_1 < 0$, $U_2 < 0$) indicates where the necessary condition for instability, $|U_1 - U_2| > 0.096$, is satisfied, but not the sufficient condition. Contour units are day^{-1}.

lower latitude than the STCC–NEC system, explains why the SSH variability from the T/P altimeter data is less energetic in the NEC band than in the STCC band.

5. Summary

Using the altimeter data from the first 5¼-yr TOPEX/Poseidon mission, we investigated the SSH fluctuations in the North Pacific Ocean. Particular attention has been paid to the region of the eastward-flowing Subtropical Countercurrent near the center of the North Pacific subtropical gyre. Embedded in the energetic wind-driven subtropical circulation, the shallow STCC has thus far not been recognized as a dynamically prominent current system. This is largely due to our lack of knowledge about the spatial and temporal changes of the STCC. The multiyear T/P altimeter data reveal that the STCC is a highly variable zonal current. Its area-averaged eddy kinetic energy level is 338 cm^2 s^{-2} and can be compared with the eddy kinetic energy level of the Kuroshio Extension at 661 cm^2 s^{-2}. This high eddy kinetic energy level suggests that the importance of the STCC in the subtropical circulation may have been underappreciated in the past.

One striking aspect of the STCC observed by the T/P altimeters is that its eddy kinetic energy level undergoes a well-defined annual cycle. The eddy kinetic energy of the STCC is maximum in April/May and minimum in December/January, with the April/May level (440 cm^2 s^{-2}) nearly doubling the level of December/January (240 cm^2 s^{-2}). No such distinct annual cycle in the eddy kinetic energy level is found in the other zonal currents of the North Pacific Ocean. In order to clarify the dynamics controlling this annual cycle, we adopted in this study a 2½-layer reduced-gravity model representing the vertically sheared STCC–NEC system. Using the parameter values appropriate for the mean state of the STCC–NEC in spring and fall, respectively, we showed that the springtime condition is considerably more favorable for baroclinic instability than the fall condition. The two factors contributing to this difference in the mean state are the vertical velocity shear of the STCC–NEC and the density difference between the STCC and NEC layers. In spring, the vertical velocity shear of the STCC–NEC is large due to the latitudinally dependent surface cooling, which steepens the isopycnals in the surface layer and reduces, at the same time, the density jump between the STCC and NEC layers. The seasonal

heating over the summer and fall seasons, on the other hand, reduces the STCC–NEC shear and increases the density jump between the STCC and NEC layers. As a result of the different mean state, the maximum growth rate for the springtime STCC–NEC is O(60 days), whereas it is O(180 days) for the fall STCC–NEC. It is this seasonal difference in the intensity of instability that modulates the eddy kinetic energy level observed in the STCC–NEC system. That the theoretically predicted e-folding timescale in spring is O(60 days) corresponds well with the time lag between the maximum STCC–NEC's shear in March and the peak eddy kinetic energy level in May (Fig. 10).

The question of how the unstable waves would evolve after the initial disturbances in the STCC–NEC attain finite amplitude, however, cannot be addressed by the linear stability analysis of this study. Existing theoretical and numerical studies suggest that the unstable waves are likely to evolve into eddies, whose length scales tend to increase through nonlinear cascade processes (Rhines 1977; Halliwell et al. 1994). The increase in eddy size ceases eventually as the eddies become large enough to disperse as baroclinic Rossby waves. Indeed, the presence of westward-propagating baroclinic Rossby waves in the STCC region has been identified in recent studies by Chelton and Schlax (1996; see their Fig. 2c) and by Aoki and Imawaki (1996). That the SSH anomalies tend to increase in amplitude westward in the band of the STCC (Fig. 1) is likely a manifestation of the eddy kinetic energy generated initially in the unstable STCC–NEC system being transferred westward by the baroclinic Rossby waves. Future studies are needed to further clarify the nonlinear evolution of these waves and to examine their impact upon the northward-flowing Kuroshio along the western boundary of the Pacific Ocean.

Another intriguing aspect of the subtropical circulation revealed by the T/P observation is the low eddy kinetic energy level associated with the westward-flowing North Equatorial Current. This is despite the fact that the NEC is a stronger vertically sheared zonal current than the STCC. That the NEC is less eddy energetic is argued in this study to be due to its presence in a low-latitude band and due to its flow being unidirectional [i.e., $U(z) < 0$ throughout the water column above the main thermocline]. For a surface-intensified zonal flow, both of these factors make the reversal of the potential vorticity gradient of the mean state, or satisfying the necessary condition for the baroclinic instability, difficult.

Finally, we comment that the high eddy kinetic energy associated with the STCC in the North Pacific Ocean resides in a zonal band (19°–25°N) south of the subtropical front. A similar frontal structure, named the subtropical convergence zone, exists in the western North Atlantic Ocean as well (Halliwell et al. 1991). As in the North Pacific, the North Atlantic subtropical front is located in the zonal band of 26°–32°N. Unlike in the North Pacific, however, the T/P altimeter data revealed no regional eddy kinetic energy maximum south of the subtropical convergence zone in the North Atlantic (see, e.g., Fig. 3a in Stammer 1997a). This result from the T/P observations raises a fundamental question about the relationship between the subtropical fronts and the subtropical countercurrents and points to the need for future studies to clarify the different behaviors of the subtropical countercurrents in different world oceans.

Acknowledgments. This study benefited from informal discussions with Drs. Eric Firing, Lee Fu, Zhengyu Liu, Douglas Luther, and Gary Mitchum. Detailed comments made by the anonymous reviewers helped clarify many parts of an early version of the manuscript. The TOPEX/Poseidon data were provided by the Physical Oceanography DAAC at JPL, California Institute of Technology. I am grateful to Dr. Gary Mitchum for help processing the original T/P data. Support from NASA through the Young Investigators Award (NAGW-5250) and the TOPEX/Poseidon Extended Mission Project (Contract 960889) is gratefully acknowledged.

REFERENCES

Aoki, S., and S. Imawaki, 1996: Eddy activities of the surface layer in the western North Pacific detected by satellite altimeter and radiometer. *J. Oceanogr.*, **52,** 457–474.

Callahan, P. S., 1993: *TOPEX/POSEIDON GDR User Handbook.* Jet Propulsion Laboratory, Special Publ. D-8944, 84 pp.

Chelton, D. B., and M. G. Schlax, 1996: Global observations of oceanic Rossby waves. *Science*, **272,** 234–238.

——, R. A. DeSzoeke, M. G. Schlax, K. E. Naggar, and N. Siwertz, 1998: Geographical variability of the first baroclinic Rossby radius of deformation. *J. Phys. Oceanogr.*, **28,** 433–460.

Cushman-Roison, B., 1984: On the maintenance of the Subtropical Front and its associated countercurrent. *J. Phys. Oceanogr.*, **14,** 1179–1190.

Denman, K. L., 1973: A time-dependent model of the upper ocean. *J. Phys. Oceanogr.*, **3,** 173–184.

Dewar, W. K., 1992: Spontaneous shocks. *J. Phys. Oceanogr.*, **22,** 505–522.

Emery, W. J., W. G. Lee, and L. Magaard, 1984: Geographical and seasonal distributions of Brunt–Väisälä frequency and Rossby radii in the North Pacific and North Atlantic. *J. Phys. Oceanogr.*, **14,** 294–317.

Fu, L.-L., 1983: On the wave number spectrum of oceanic mesoscale variability observed by the SEASAT altimeter. *J. Geophys. Res.*, **88,** 4331–4341.

——, E. J. Christensen, C. A. Yamarone, M. Lefebvre, Y. Menard, M. Dorrer, and P. Escudier, 1994: TOPEX/POSEIDON mission overview. *J. Geophys. Res.*, **99,** 24 369–24 381.

Halliwell, G. R., Jr., Y. J. Ro, and P. Cornillon, 1991: Westward-propagating SST anomalies and baroclinic eddies in the Sargasso Sea. *J. Phys. Oceanogr.*, **21,** 1664–1680.

——, G. Peng, and D. B. Olson, 1994: Stability of the Sargasso Sea Subtropical Frontal Zone. *J. Phys. Oceanogr.*, **24,** 1166–1183.

Hasunuma, K., and K. Yoshida, 1978: Splitting the subtropical gyre in the western North Pacific. *J. Oceanogr. Soc. Japan*, **34,** 160–172.

Kubokawa, A., 1997: A two-level model of subtropical gyre and Subtropical Countercurrent. *J. Oceanogr.*, **53,** 231–244.

Le Traon, P. Y., M. C. Rouquet, and C. Boissier, 1990: Spatial scales

of mesoscale variability in the North Atlantic as deduced from Geosat data. *J. Geophys. Res.,* **95,** 20 267–20 285.

Levitus, S., and T. Boyer, 1994: *World Ocean Atlas 1994.* Vol 4, *Temperature.* NOAA Atlas NESDIS 4, U.S. Govt. Printing Office, 117 pp.

——, R. Burgett, and T. Boyer, 1994: *World Ocean Atlas 1994.* Vol 3, *Salinity.* NOAA Atlas NESDIS 3, U.S. Govt. Printing Office, 99 pp.

Liu, Z., 1999: Planetary wave modes in the thermocline: Non-Doppler-shift mode, advective mode and Green mode. *Quart. J. Roy. Meteor. Soc.,* **125,** 1315–1339.

McCreary, J. P., H. S. Lee, and D. B. Enfield, 1988: The response of the coastal ocean to strong offshore winds: With application to circulations in the Gulfs of Tehuantepec and Papagayo. *J. Mar. Res.,* **47,** 81–109.

Pedlosky, J., 1987: *Geophysical Fluid Dynamics.* Springer-Verlag, 710 pp.

Qiu, B., 1995: Variability and energetics of the Kuroshio Extension and its recirculation gyre from the first two-year TOPEX data. *J. Phys. Oceanogr.,* **25,** 1827–1842.

Rhines, P. B., 1977: The dynamics of unsteady currents. *The Sea.* Vol. 6, E. D. Goldberg, I. N. McCane, J. J. O'Brien, and J. H. Steele, Eds., Wiley Interscience, 189–318.

Roden, G. I., 1975: On the North Pacific temperature, salinity, sound velocity and density fronts and their relation to the wind and energy flux fields. *J. Phys. Oceanogr.,* **5,** 557–571.

——, 1980: On the variability of surface temperature fronts in the western Pacific, as detected by satellite. *J. Geophys. Res.,* **85,** 2704–2710.

Semtner, A. J., and R. M. Chervin, 1992: Ocean general circulation from a global eddy-resolving model. *J. Geophys. Res.,* **97,** 5493–5550.

Stammer, D., 1997a: Global characteristics of ocean variability estimated from regional TOPEX/Poseidon altimeter measurements. *J. Phys. Oceanogr.,* **27,** 1743–1769.

——, 1997b: Steric and wind-induced changes in TOPEX/Poseidon large-scale sea surface topography observations. *J. Geophys. Res.,* **102,** 20 987–21 009.

Stumpf, H. G., and R. V. Legeckis, 1977: Satellite observations of mesoscale eddy dynamics in the eastern tropical Pacific Ocean. *J. Phys. Oceanogr.,* **7,** 648–658.

Takeuchi, K., 1984: Numerical study of the Subtropical Front and the Subtropical Countercurrent. *J. Oceanogr. Soc. Japan,* **40,** 371–381.

——, 1986: Numerical study of the seasonal variations of the Subtropical Front and the Subtropical Countercurrent. *J. Phys. Oceanogr.,* **16,** 919–926.

Uda, M., and K. Hasunuma, 1969: The eastward Subtropical Countercurrent in the western North Pacific Ocean. *J. Oceanogr. Soc. Japan,* **25,** 201–210.

Welander, P., 1981: Mixed layer and fronts in simple ocean circulation model. *J. Phys. Oceanogr.,* **11,** 148–152.

White, W., K. Hasunuma, and H. Solomon, 1978: Large scale season and secular variability of the Subtropical Front in the western North Pacific from 1954 to 1974. *J. Geophys. Res.,* **83,** 4531–4544.

Wyrtki, K., 1975: Fluctuations of the dynamic topography in the Pacific Ocean. *J. Phys. Oceanogr.,* **5,** 450–459.

Yoshida, K., and T. Kidokoro, 1967: A subtropical countercurrent (II)—A prediction of eastward flows at lower subtropical latitudes. *J. Oceanogr. Soc. Japan,* **23,** 231–246.

Yuan, X., and L. D. Talley, 1996: The subarctic frontal zone in the North Pacific: Characteristics of frontal structure from climatological data and synoptic surveys. *J. Geophys. Res.,* **101,** 16 491–16 508.